THE JOURNAL OF PHYSICAL CHEMISTRY A

Article

pubs.acs.org/JPCA

Fluorescence-Detected X-ray Magnetic Circular Dichroism of Well-Defined Mn^{II} and Ni^{II} Doped in MgO Crystals: Credential Evaluation for Measurements on Biological Samples

Hongxin Wang,*[,†,‡] Craig Bryant,[†,‡] M. LeGros,[‡] Xin Wang,[†,‡,§] and S. P. Cramer*[,†,‡]

[†]Department of Chemistry, University of California, Davis, California 95616, United States

[‡]Lawrence Berkeley National Laboratory, Berkeley, California 94720, United States

ABSTRACT: $L_{2,3}$-edge X-ray magnetic circular dichroism (XMCD) spectra have been measured for the well-defined dilute Ni^{II} and Mn^{II} ions doped into a MgO crystal, with sub-Kelvin dilution refrigerator cooling and 2 T magnetic field magnetization. A 30-element Ge array X-ray detector has been used to measure the XMCD for these dilute ions, whose concentrations are 1400 ppm for Ni^{II} and 10 000 ppm for Mn^{II}. Large XMCD effects have been observed for both Ni^{II} and Mn^{II}, and multiplet simulation described the observed spectra. The fluorescence-detected L-edge absorption spectrum and XMCD of Ni^{II} in MgO are comparable with both theoretical calculations and the total electron yield measured ions in similar chemical environments, at least qualitatively validating the use of the sensitive fluorescence detection technique for studying XMCD for dilute 3d metal ions, such as various metalloproteins. Sum rule analyses on the XMCD spectra are also performed. In addition, these XMCD measurements have also been used to obtain the sample's magnetization curve and the beamline's X-ray helicity curve. This study also illustrated that bend magnet beamlines are still useful in examining XMCD on dilute and paramagnetic metal sites.

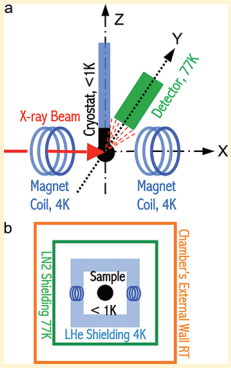

1. INTRODUCTION

X-ray magnetic circular dichroism (XMCD) measures the X-ray absorption difference between the left and the right circularly polarized X-ray beams in the presence of a magnetic field. It has been developed as a powerful element and site-specific probe of electronic and magnetic structures in various fields.[1−6] Through ligand field multiplet simulations[7−11] and the application of X-ray sum rules,[12,13] predictions can be made about the electronic configuration as well as the orbital and spin angular momentum for a particular element present in the probing sample. XMCD spectroscopy is now a well-established technique for materials sciences[3,5,6,14,15] and even for some biological sciences.[16−18]

Since the first X-ray crystal structure report on iron-containing sperm whale myoglobin in 1950s, the X-ray probe of metalloproteins has attracted chemists, biochemists, as well as other scientists for decades[19] Measuring metals inside of biological samples has several practical issues. First, biological metals are dilute in concentration, for example, one myoglobin molecule (17 KDa) has only one iron, leading to 0.33% iron concentration (by weight). Therefore, sensitive fluorescence detection has to be employed to extract the weak metal signal from the dilute samples. Questions have been raised as to the accuracy of fluorescence-detected X-ray absorption spectra.[20−23] Although some previous theoretical work suggests that the problem is for the rare earth elements and that the X-ray fluorescence detection should be valid for 3d transition-metal complexes[24] and X-ray fluorescence detected XAS on biological 3d metals[17,18,20,21] have been reported, it is still important to evaluate the X-ray fluorescence detect on some well-defined standard systems.

Second, unlike ferromagnetic materials, metal sites in biological samples are paramagnetic. Therefore, an ultrahigh magnetic field (B, in the level of Teslas) and an ultralow cryogenic temperature (T, in the level of Kelvin or sub-Kelvin) have to be employed to effectively align the paramagnetic moments inside of the metalloprotein samples. The magnetic saturation extent is an exponential function of B/T, and B/T = 4 is needed for an almost full magnetization of a spin = 1 paramagnetic moment (the metal centers inside of biological samples). Nevertheless, the dilute samples' real magnetic saturation level still better be calibrated experimentally with well-defined standard systems.

In this paper, two well-defined samples, Mn^{II} and Ni^{II} ions doped into single MgO crystals,[25] were used to examine the fluorescence-detected XMCD and to examine the magnetic saturation. The observed XMCD spectra were simulated with the ligand field multiplet calculations[20,22] and examined against the XMCD sum rules.[17] The Ni XMCD spectra obtained here are comparable to the previously reported total electron yield (TEY) measured XMCD spectra on similar ferromagnetic Ni materials.[26,27] These XMCD spectra were also used as an indicator to study and calibrate the samples' magnetic saturation curves and the beamline's X-ray helicity curves. All of these illustrated well that the X-ray fluorescence-detected XMCD is valid, at least for the later 3d metal ions (e.g. Ni). This is the first report of XMCD on a well-defined, dilute, and paramagnetic metal ion system.

Received: March 22, 2012
Revised: May 25, 2012
Published: May 31, 2012

Of course, real metalloproteins have various local symmetries (e.g., O_h, T_d, square planar, tetragonal, etc.), various ligands (S, N, C, as well as O), and the even more complicated environment beyond the first-layer ligands. All of these aspects affect the details of X-ray absorption spectra or XMCD spectra. The doped Ni and Mn in MgO used in this study have only O_h symmetry and only O ligands and thus cannot represent the real biological metals in every detail. However, these standard samples do have some generalized similarities with the biological metal sites: (1) both have a localized metal−ligand interaction; (2) both have dilute metal ions; and (3) both have paramagnetic metal ions, which are not coupled with the neighboring metal sites. These similarities, along with their simplicity, well-defined properties, and the chemical stability, make them useful standards samples for evaluating and calibrating the XMCD measurements on real biological metals.

2. EXPERIMENTS

A. Samples. Samples of Ni^{II} and Mn^{II} doped into a single crystal MgO were obtained from Goodfellow Metals, Inc. and used without further treatment. Both doped crystals were flat plates with a smooth (001) surface. In our XMCD experiments, the crystals were attached to a gold-plated sample holder with silver paint to achieve good thermal conductivity. The incoming X-ray beam made an angle of 55° with respect to the samples' normal (a C_{4v} or 001 axis). The Ni^{II} dopant concentration was 0.14% (1400 ppm by weight), while the Mn doped sample contained 1% Mn. These concentration levels resemble the small to intermediate (5−50 KDa per metal site) sized metalloproteins found in nature, such as rubredoxin (6 KDa, 0.93% iron)[28] and myoglobin (17 KDa, 0.33% iron).[20] Previous EPR work[25,29] showed that the Mn^{II} and Ni^{II} local environments are essentially octahedral in the center of six O ligands and that the doped Ni/Mn substitute for Mg sites in MgO crystals. The Ni^{II} dopant has $S = 1$, while the Mn^{II} has $S = 5/2$ for the ground states. These two well-defined metal models are good "calibration" systems for testing and evaluating the credence of the fluorescence-detected XMCD of a super high field produced magnetic saturation, as well as of other experimental issues for dilute 3d metal systems in general (e.g., for various metalloprotein molecules).

B. XMCD Instrument. The advanced XMCD apparatus, built in collaboration with Janis Instruments, uses a 76 cm split-coil 2 T superconducting magnet surrounded by a UHV chamber (maintained at ~5×10^{-9} Torr), a ^{3}He/^{4}He dilution refrigerator insert (Janis Research, MK-400T), and a 30-element Ge fluorescence detector (Canberra Industries, GUL0055). The detector is inserted horizontally between the two coils, perpendicular to the photon beam path under windowless operation.[16,17] The overview of the XMCD setup is as shown in Figure 1a. The maximum magnetic field is $B = 2$ T in this apparatus; and we did not observe significant "field-induced" degradation of detector performance with the detector placed 3 in. from the sample. At this distance, the solid angle and the overall count rate/resolution were also optimized for the whole detector array. The signal pulses from the Ge detector were amplified with Canberra 2026 amplifiers (using 3 μs shaping times) and sequenced with eight Canberra 8224 multiplexers. Peak heights were then analyzed with eight Canberra 8715 analogue to digital converters (ADCs). The resulting histogrammed pulses were stored in the memory on a DEC Alpha 3000 computer. One integration region was defined around the Mn or Ni fluorescence signal (F). A second window was selected around the oxygen fluorescence. The oxygen signal was used as a measure of the incident intensity (I_0). The raw spectrum was then collected as (F/I_0) versus the excitation energy (E). The energy was calibrated with NiF_2 and MnF_2.

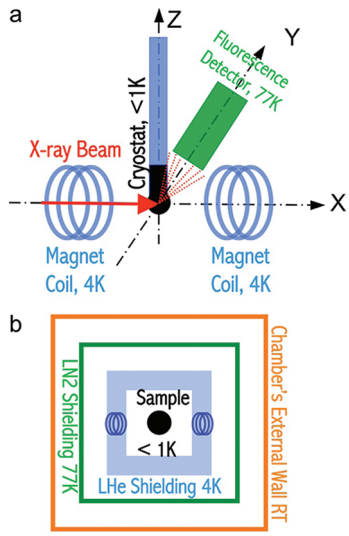

Figure 1. (a) The schematic overview of the XMCD setup; (b) the cross section at the sample level. The temperatures are illustrated as sample at <1 K (black); magnet and cryostat's intermediate layer at 4 K (blue); and X-ray fluorescence detector and chamber's LN2 shields at 77 K (green).

The ^{3}He/^{4}He dilution refrigerator insert enters the magnet bore from the top of the chamber, and the sample is attached to the coldfinger at the center of the magnet bore (Figure 1a). The ^{3}He/^{4}He dilution refrigerator achieves an ultralow temperature by continuous evacuation and cycling of ^{3}He from a ^{3}He + ^{4}He mixture.[30] Around the sample/coldfinger, a 4 K liquid helium (LHe) shielding and a 77 K liquid nitrogen (LN2) shielding were used to minimize the coldfinger's thermal load. Samples were introduced into the magnet bore through a vacuum load-lock and screwed onto the coldfinger using a removable sample insertion device. Samples with sample holder were precooled to the LN2 temperature inside the UHV load-lock environment prior to being loaded into the XMCD chamber to minimize the thermal impact of the "warm" samples to the coldfinger. The 4 and 77 K as well as the apparatus's other temperature zones were illustrated as shown in Figure 1b. The LHe shields have entrance and exit holes and polypropylene thermal shielding widows for the incoming X-ray beam and for the outgoing fluorescence emission signal. The thermal shielding is critical to reduce the room-temperature thermal load and maintain the samples at sub-Kelvin temperatures.

The temperature on the coldfinger was monitored down to 1.4 K with a Lakeshore DT-470-12A silicon diode. The temperature between 50 mK and 4.2 K was measured using a calibrated Matsushita carbon resistance thermometer. The sample's real temperature can also be determined (confirmed) by the analysis of sample magnetization curves, as will be described later. The operating temperature in our experiments was about 0.5 K. Periodic magnetic field reversal is required to modulate the sign of the XMCD. To avoid excessive heat impact to the dilution fridge during this procedure (via eddy current heating of the coldfinger), a moderate magnetic field

dx.doi.org/10.1021/jp3027622 | J. Phys. Chem. A 2012, 116, 10082−10089

sweep rate of 50 g/s was used, and this kept the corresponding temperature rise to less than 100 mK per switch. The temperature recovered to the equilibrium (0.5 K) in five minutes after a field change; at this time, the XMCD measurement could be resumed.

C. Data Collection. The XMCD experiments were performed at the SSRL bend magnet beamline 8-2[31,32] using the 1100 L/mm grating. Elliptically polarized X-rays were obtained by moving the first mirror above or below the electron orbit plane. On the basis of previous calibration experiments on polarized ferromagnetic samples, the optimum XMCD signal was obtained at a beam takeoff angle corresponding to a circular polarization of 80 ± 5%. At this takeoff angle, the beam intensity is about 25% of its maximum intensity. As described below, this value was later checked by comparison of theoretical and experimental polarization estimated on the Ni^{II} doped MgO sample. The entrance and exit slits were both set to 50 μm, and the energy resolution was estimated to be 1.2 eV at the Ni L-edge and 0.8 eV at the Mn L-edge for the circularly polarized beam. The oxygen fluorescence measured I_0 signal was checked to be proportional to the incident flux (measured with a gold mess) to a good approximation.

Individual scans were taken over the metal L-edges using 0.2 eV steps at 5 s per point integration time. One set of 16 scans was taken with right circular polarization. Every two scans, the magnetic field was switched between −2 and +2 T. A second set of 16 scans was then taken with left circular polarization, again alternating the sign of the magnetic field. The apparent XMCD effect did reverse with opposite beam polarization. For measurement of the magnetization curves, a similar procedure was followed, collecting only the L_3-edge region using a magnetic field between 0.1 and 2.0 T. For the polarization curves, the XMCD measurements were done (again, the L_3-edge only at a fixed field of 2 T) at different mirror positions, corresponding to different takeoff angles above and below the ring orbital plane. As a convention, the mirror position reading (motor steps) was first converted to the observation angle ψ (in mili-radians) and then converted to $\gamma\psi$,[33] by multiplying ψ by a factor of γ = electron energy/rest energy = 3 GeV/0.511 MeV = 5870.84 (which is a SSRL parameter).

The model compound NiF_2 was measured at ALS beamline 4.0.2 using a published regular procedure with a channeltron. For comparison, the regular L-edge XAS Ni^{II}/MgO was also measured at ALS beamline 4.0.2 at 4 K with a 30-element X-ray fluorescence detector (Canberra Industries, GUL0055). The Ni^{II}/MgO L-edge XAS such measured was very similar to the averaged XMCD spectrum $(I^{\uparrow\uparrow} + I^{\uparrow\downarrow})/2$ measured at SSRL BL8-2 (as described above).

D. Data Analysis. L-edge excitation spectra (F/I_0) taken with the X-ray photon angular momentum either parallel $(I^{\uparrow\uparrow})$ or antiparallel $(I^{\uparrow\downarrow})$ to the angular momentum of the metal ion were first added together (16 scans each side). Then, each spectrum was normalized to the edge jump between the pre-L_3- and post-L_2-edge and then corrected for the small energy offset between spectra recorded on opposite sides of the orbital plane. A double step curve was then fit to the raw data (F/I_0) in the pre-L_3- and post-L_2 regions to simulate and remove the two-step nonresonant background of the spectra. Finally, the parallel and antiparallel absorption spectra were corrected for the fact that the illuminating X-rays were only 80% polarized by

$$I^{\uparrow\uparrow} = [(\alpha + 1)I^{\uparrow\uparrow}{}_m + (\alpha - 1)I^{\uparrow\downarrow}{}_m]/2\alpha \quad (1)$$

$$I^{\uparrow\downarrow} = [(\alpha + 1)I^{\uparrow\downarrow}{}_m + (\alpha - 1)I^{\uparrow\uparrow}{}_m]/2\alpha \quad (2)$$

$$\mathrm{XMCD} = (I^{\uparrow\uparrow} - I^{\uparrow\downarrow})/(I^{\uparrow\uparrow} + I^{\uparrow\downarrow}) = [(I^{\uparrow\uparrow}{}_m - I^{\uparrow\downarrow}{}_m)/(I^{\uparrow\uparrow}{}_m + I^{\uparrow\downarrow}{}_m)]/\alpha \quad (3)$$

where the $I^{\uparrow\uparrow}{}_m$ and $I^{\uparrow\downarrow}{}_m$ represent the observed spectra while the $I^{\uparrow\uparrow}$, $I^{\uparrow\downarrow}$, and XMCD are the polarization-corrected intensities, α is the beam's polarization.

The multiplet simulations[7−11] for the observed XAS spectra were performed by published methods. For Ni^{II}, the calculation involves electronic transitions from the $3d^8$ ground state to the $2\underline{p}^5 3d^9$ excited state, where $2\underline{p}^5$ stands for the 2p core hole. For Mn^{II}, the calculation simulates electronic transitions from a $3d^5$ ground state to a $2\underline{p}^5 3d^6$ excited state. Coulomb, exchange, and spin−orbital interactions for both initial and final states were first calculated. The atomic multiplet approximation was used to calculate the ground and final state spin−orbital L−S interactions and the final state 2p core hole J−J coupling. The *ab initio* Hartree−Fock values of Slater integrals and spin−orbital couplings for the 3d transition metals used were tabulated values.

The calculated atomic multiplets were expressed as eigenstates appropriate for the ion in a ligand field. XMCD selection rules were imposed on the transitions to obtain the XMCD spectra. The local symmetry of the Ni and Mn sites in MgO was assumed to be O_h symmetry. In O_h symmetry, the 3d orbitals are split into t_{2g} and e_g representations with an energy difference of 10 D_q. The appropriate values for 10 D_q were optimized by comparing the calculated with the experimental spectra. The calculated spectra were convoluted with Lorentzian and Gaussian line shapes to account for the lifetime and instrumental broadening, respectively.

3. RESULTS AND DISCUSSION

A. XMCD and Multiplets. The Ni L-edge excitation spectra for Ni/MgO ($I^{\uparrow\uparrow}$ and $I^{\uparrow\downarrow}$) are reported in Figure 2a. The spectra are typical of previously reported high-spin (triplet state) Ni^{II},[21,27,34] which can be well-described by ligand field multiplet simulations. The L_3 region has a major peak near 853.4 eV, a minor peak near 855.6 eV, and some broad structure near 859−862 eV. Arrio and co-workers[26,34] have shown that the latter satellite structure requires inclusion of configuration interaction with $3d^9\underline{L}$ character in the ground state in the calculations. The L_2 at 869−873 eV has a partially resolved doublet structure (peaks at 870.0 and 871.6 eV). The overall feature is similar to the Ni^{II} ion inside of the magnetic material of $Cs(Ni^{II}Cr^{III}(CN)_6)\cdot 2H_2O$.[26,27] The multiplet simulation with 10 D_q = 1.0 eV reproduces the measured spectra (Figure 2b).

It is well recognized that significant spectral distortion occurs in the fluorescence detection of the f shell rare earth materials.[35,36] Although some work mentioned the possible distortion in 3d metals, our spectra for the dilute (0.14%) Ni^{II} ion do not show a significant distortion effect. The ratio of L_3 to L_2 peak heights is about 4:1, which agrees well with previous TEY results (also 4:1) on high-spin Ni^{II} compounds in the reports[26,27] and in our own measurements (Figure 3). The ratio of the two L_3 subpeaks (slightly smaller than 4:1) also resembles the previously published or measured TEY results (4:1), suggesting no obvious fluorescence detection distortion. These data are listed in Table 1. The averages of ↑↑ and ↑↓ for Ni^{II}/MgO were also compared with the TEY measured Ni^{II} in

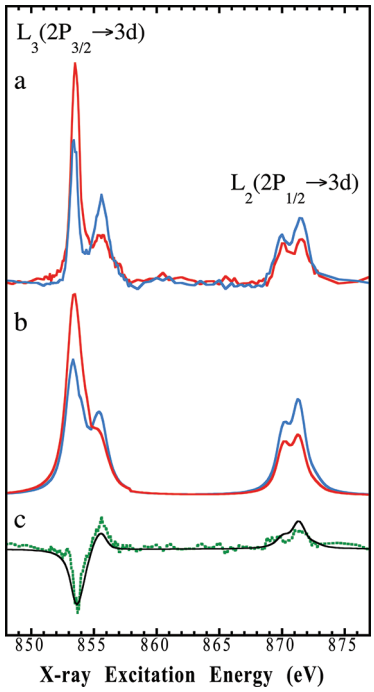

Figure 2. (a) Normalized, background-subtracted Ni fluorescence-detected spectra for Ni^{II}/MgO, taken with the photon angular momentum parallel (red line) and antiparallel (blue line) to the transition metal 3d spin; (b) calculated XAS spectra of Ni^{II}/MgO for the photon angular momentum parallel (red) and antiparallel (blue) to the 3d spin; (c) observed (dotted green line) and calculated (solid black line) XMCD spectrum for Ni/MgO.

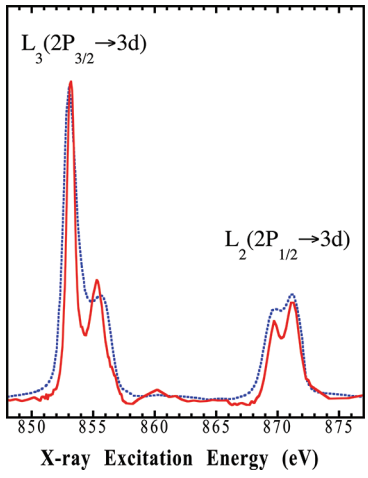

Figure 3. Fluorescence-detected L-edge absorption spectra (averaged $(I^{\uparrow\uparrow} + I^{\uparrow\downarrow})/2$) of Ni^{II} doped in MgO (solid red line) and the TEY measured Ni^{II} ion in NiF_2 (dotted blue line).

the ionic NiF_2 complex in the same L-edge region (Figure 3).[37] The overall close match of the two spectra again provides credibility for fluorescence detection at low concentration, such as 0.14% Ni.

Shown in the bottom portion (dotted line) of Figure 2 is the polarization-corrected difference in fluorescence signals ($I^{\uparrow\uparrow} - I^{\uparrow\downarrow}$), which is proportional to the X-ray magnetic circular dichroism effect (XMCD). At the L_3-edge peak, there is a 44% difference in polarization-corrected fluorescence intensity between the two peaks (corresponding to a 22% XMCD effect). This is not far from the previously reported 60%

Table 1. Comparison of X-ray Fluorescence Yield Detected XAS and XMCD Properties for Ni^{II}/MgO in this Study and TEY Measured Ni^{II} in $Cs(NiCr(CN)_6)\cdot 2H_2O$ in the Previous Reports[26,27]

measurements	FY detected	TEY detected
samples	Ni doped in MgO	$Cs(NiCr(CN)_6)\cdot 2H_2O$
states	Ni(II, HS), O_h	Ni(II, HS), O_h
XAS: L_3	doublet, 3.7:1	doublet, 4:1
XAS: L_2	doublet, 1:1	doublet, 1:1
XAS: L_3/L_2	4:1	4:1
XMCD: L_3	bipolar, 44%	bipolar, 60%
L_3(maj/min)	3.5:1	4:1
XMCD: L_2	unipolar, 8%	unipolar, 30%
L_2(maj/min)	1.5:1	1.7:1
SR: $\langle S_z \rangle$	0.38	0.40
SR: $\langle L_z \rangle$	0.03	0.10

absorption difference for Ni^{II} ions in $Cs(NiCr(CN)_6)\cdot 2H_2O$.[26,27] The differences are kind of expected because (1) there was a much larger correction for the degree of circular polarization in the previous report;[26,27] (2) their averaged signal was $(L + R + z)/3$ while ours is $(L + R)/2$ instead; and (3) their sample was an unoriented powder while our sample is a (001) oriented single crystal. Nevertheless, our measurement is qualitatively consistent with theirs while also in close agreement with the ligand field calculation with 10 D_q = 1 eV (Figure 2b and c). The XMCD in the L_2 peak is unipolar, also consistent with the $Cs(NiCr(CN)_6)\cdot 2H_2O$ reports.[26,27] The XMCD effect at L_2 is about 8%.

A bipolar XMCD signal was observed in the L_3 peak with an intensity ratio of 3:1, which is close to the 3.5:1 for Ni^{II} in Arrio et al.'s molecular magnets.[26,27] This effect is nicely reproduced in the spectral simulations of a typical Ni^{II} ($^3A_2$) ground state in O_h symmetry. This can be understood qualitatively as follows. The L absorption corresponds approximately to an excitation to a $2p^5 3d^9$ final state, with J = 3/2 or 1/2 core hole spin to further split the transition into L_3 and L_2. The signals at the L_3 have opposite signs because the main L_3 peak corresponds to excitations with the final $2p^5$ spin parallel to the $3d^9$ spin, while the shoulder is the transition with the final $2p^5$ spin antiparallel to the $3d^9$ spin. This is always the case unless there is a strong distortion (like in D_{2h} or other low symmetries), which could then cancel out some of the shoulder features.

In previous studies on $Fe_5Gd_3O_{12}$ garnets,[38] the presence of peaks with an opposite sign of the XMCD effect was interpreted as arising from the antiferromagnetic coupling between the tetrahedral and octahedral Fe sites. There is no reason to question that interpretation. However, the Ni results show that there is no simple correspondence between the sign of a peak and the presence of a component in the sample with a particular magnetic coupling. For interpretation of the XMCD of Ni complexes, simulations becomes essential to distinguish between detailed small effects and possible artifacts.

The fluorescence-detected XMCD spectrum for Mn/MgO was recorded as in Figure 4. At the L_3-edge maximum, there is a 50% difference in polarization-corrected intensities, corresponding to a 25% XMCD effect. There is also very rich multiplet structure that is only partially resolved at the beamline resolution. As with Ni/MgO at L_3, the secondary peak has an XMCD of opposite sign to the main peak. However, the spectra are too complex for a simple interpretation because of the d^5 configuration of Mn^{II}. Unfortunately the strong Mg second-

dx.doi.org/10.1021/jp3027622 | J. Phys. Chem. A 2012, 116, 10082−10089

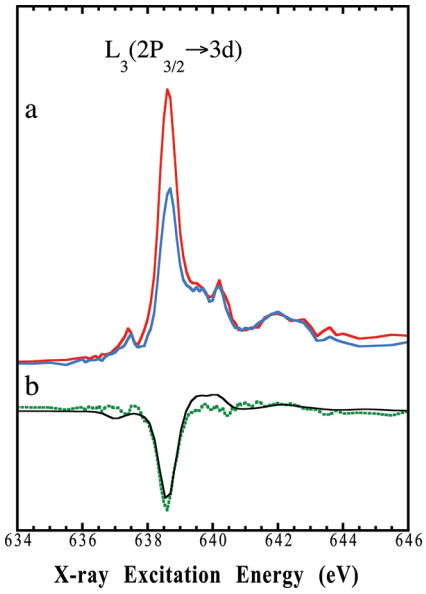

Figure 4. (a) Normalized, background-subtracted Mn fluorescence-detected spectra for Mn^{II}/MgO, taken with the photon angular momentum parallel (red line) or antiparallel (blue line) to the transition metal 3d spin. (b) Observed (dotted green line) and calculated (solid black line) XMCD spectra for Mn^{II}/MgO.

order K-edge absorption (1303 → 651.5 eV) overlaps with the L_2-edge of Mn ^{II} (650 eV); therefore, no spectrum has been obtained in the Mn L_2 region for Mn^{II}/MgO. The simulations again reproduce both the sign and amplitude of the XMCD structure with O_h symmetry (10 D_q = 0.9 eV).

B. XMCD Sum RuleS. There are two important XMCD sum rules[12,13,17] that relate the integrated XMCD intensities to element-specific projections of the 3d orbital angular momentum $\langle L_z\rangle$, the 3d spin angular momentum $\langle S_z\rangle$, and a magnetic dipole term $\langle T_z\rangle$. For 3d transition-metal L-edges, to better apply these XMCD sum rules, the following integrals are defined

$$A = \int_{L_3} (I^{\uparrow\uparrow} - I^{\uparrow\downarrow})\, d\omega \qquad B = \int_{L_2} (I^{\uparrow\uparrow} - I^{\uparrow\downarrow})\, d\omega$$
$$C = \int_{L_3+L_2} [(I^{\uparrow\uparrow} + I^{\uparrow\downarrow})/2]\, d\omega \tag{4}$$

where ω is the incident photon energy and L_i (i = 2, 3) denotes the integral range. The corresponding integrals are illustrated in Figure 5. With these integrals

$$\langle L_z\rangle = -n_h[(A + B)/2C]$$
$$\langle S_z\rangle = -(3/2)n_h[(A - 2B)/2C](1 + (7/2)\langle T_z\rangle/\langle S_z\rangle)^{-1} \tag{5}$$

Here, n_h represents the number of 3d vacancies in the metal ion. As these doped samples are oriented, the last term containing $\langle T_z\rangle$, in general, cannot be averaged to zero as for the "powder" samples. However, Arrio and co-workers pointed out that this term is often very small for the highly symmetric (octahedral) Ni^{II} ions as well.[26,27] Omitting the $\langle T_z\rangle$ term and using the common symbols in the XMCD literature (A, B, and C),[17,39] the XMCD sum rules can be re-expressed in the following manner, in units of $\hbar$ per atom

$$\langle L_z\rangle = -n_h[(A + B)/2C]$$

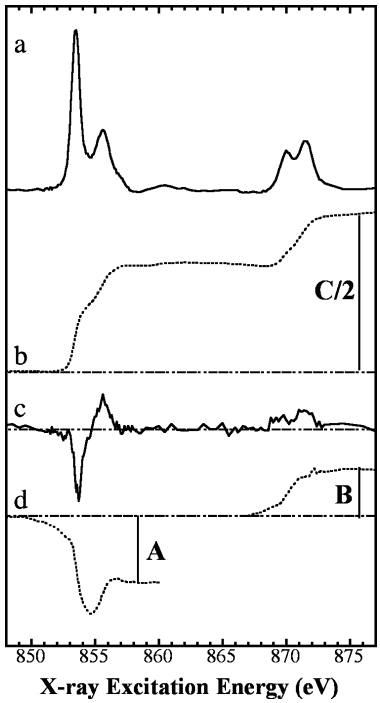

Figure 5. Averaged absorption spectrum, $(I^{\uparrow\uparrow} + I^{\uparrow\downarrow})/2$, of Ni^{II} ions doped in MgO (a), followed by its integration curve over the whole L-edge (b, labeled C/2), the XMCD spectrum (c), and the XMCD integration curve over the L_3 and L_2 regions, respectively (d, labeled A and B).

$$\langle S_z\rangle = -(3/2)n_h[(A - 2B)/2C] \tag{6}$$

As illustrated in Figure 5, A = 4.5 ± 0.3, B = −3.0 ± 0.2, and C = 20.8 ± 0.6. Using a value of 1.8 for n_h (assuming 90% covalency) in the calculations, we found $\langle L_z\rangle$ and $\langle S_z\rangle$ to be 0.06 ± 0.02 and 0.68 ± 0.06, respectively. The number for the $\langle L_z\rangle$ and $\langle S_z\rangle$ per n_h were also derived as 0.03 ± 0.01 and 0.38 ± 0.03. The error analysis is based on the statistical error plus 10% instrumental error. The ratio of $\langle L_z\rangle/\langle S_z\rangle$ is ∼0.08, regardless of the number of holes n_h. These sum rule analyzed values are summarized in Table 1, along with reported results for a TEY measured Ni^{II} ion. Besides the many other similarities in between the L-edge absorption/XMCD spectra for Ni^{II}/MgO and for the Ni^{II} ions inside of $Cs(NiCr(CN)_6)\cdot 2H_2O$,[26,27] the above calculated spin angular momenta for these two Ni^{II} ions have comparable values (0.38$\hbar$ versus 0.40$\hbar$). However, more difference exists for the orbital angular momenta between them (0.03$\hbar$ versus 0.10$\hbar$).

C. Magnetization Curves. The samples' magnetization was also investigated by analyzing the field-dependent XMCD effects, as shown in Figure 6. As expected, the spin 5/2 Mn^{II} ion shows a much steeper magnetization curve (magnetization versus B/T) than the spin 1 Ni^{II}, which is then steeper than the spin 1/2 Cu^{II} (from a previous experiment[17]). For more quantitative understanding, we fit these magnetization data to a Brillion function as below.[40]

$$R = \mathrm{XMCD}/(\mathrm{XMCD})_{max}$$
$$= (2J + 1)/(2J)*\coth[(2J + 1)a/2] - 1/(2J)$$
$$*\coth(a/2) \tag{7}$$

in which $x = (\mu_B B/kT)$, $a = gx$, $\coth(a) = (e^x + e^{-x})/(e^x - e^{-x})$ and $g = 1 + [J(J + 1) + S(S + 1) - L(L + 1)]/2J(J + 1)$, which

dx.doi.org/10.1021/jp3027622 | J. Phys. Chem. A 2012, 116, 10082−10089

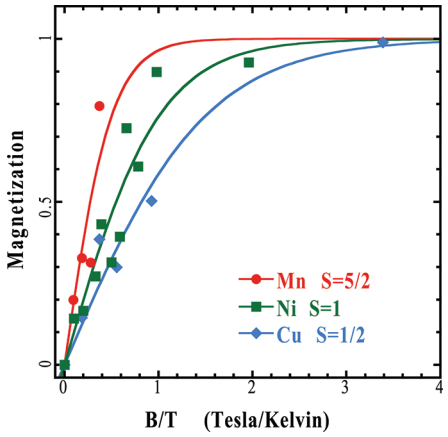

Figure 6. Experimental magnetization curve measured with the XMCD effect (solid symbols) as a function of the ratio of the magnetic field over the temperature (B/T), along with a Brillouin function fit (solid line).

is called the Lande factor. In the formula, μ_B is the Bohr magnetron, k the Boltzmann constant, B the magnetic field, and T the sample's temperature. As the orbital angular momentum for a ligand chemical complex should be close to zero in comparison with its spin contribution, for the first-order approximation, we omit L and let $J = S$ and $g = 2$ approximately. Under this special circumstance ($L = 0$, $g = 2$), we obtain

$$R = (2S + 1)/(2S)*\coth[(2S + 1)x] - 1/(2J)*\coth(x) \quad (8)$$

A least-squares fit of our measured XMCD data (using the temperature from the reading, 0.5 K) to eq 8 yields estimated spin values of 0.4$\hbar$, 0.9$\hbar$, and 2.0$\hbar$ per metal ion. Although the spin values are not equal to the nominal values, their ratio 0.4:0.9:2.0 is very close to the nominal values 0.5:1.0:2.5 (=0.4:0.8:2.0). The error may come from the estimation of the sample temperature, including the absolute scale of the temperature reading as well as the slightly different temperatures for different samples. The errors could also be from the XMCD measurement/analysis error and/or an oversimplified model for L and g values. Nevertheless, the magnetization curves may be a very useful tool to distinguish different spin species under the same experimental conditions. By using the nominal spin values, the temperature for this study is estimated to be 0.45 K. This assumes that other second-rank tensor zero field splitting(s) do not dominate the ground-state spin Hamiltonian. Although the temperature estimation depends on the spin value as well as the zero field splitting(s) in the ground state, the estimation for the magnetic saturation is directly from the observed magnetization curve and is not affected by these factors. In our XMCD measurement, a 99% magnetic saturation is achieved for the Ni^{II} doped MgO crystal.

D. Helicity Curves. Under conditions of constant sample temperature (0.5 K) and constant magnetic field (2 T), the magnitude of the XMCD effect is directly proportional to the helicity of the incoming X-ray photons. The XMCD of Ni^{II} was measured at different first mirror positions (in the beamline) to examine the degree of beam polarization at different "out-of-plane" observation angles (ψ or $\gamma\psi$). The measured XMCD effect for Ni^{II} is shown as in Figure 7b (solid symbols), and the corresponding beam intensities (measured with a gold grid) are also shown in Figure 7a. These data constitute the basis for estimating the degree of polarization at a given mirror position.

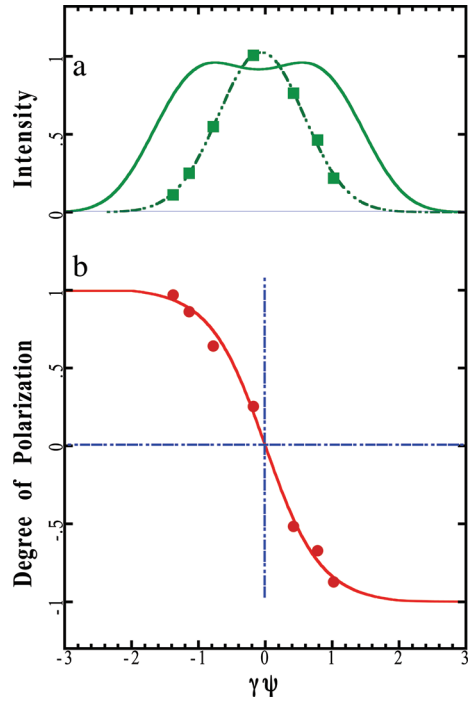

Figure 7. (a) X-ray beam intensity at different out-of-plane observation angles ($\gamma\psi$) (green square symbols) measured with a gold grid at bent magnet SSRL BL8.2, along with a simple Gaussian fit (dotted−dashed green line) and the theoretical prediction (solid green line); (b) the degree of polarization at different $\gamma\psi$ measured with fluorescence detection on Ni^{II}/MgO XMCD (red round solid symbols), along with the theoretical prediction of the degree of polarization (solid red line).

To better understand the observations, the degree of polarization for radiation from a bend magnet was calculated theoretically by solving modified Bessel functions.[33] The horizontal (E_x) and vertical (E_y) components of the electric fields were followed by calculation of circular polarization $P = 2r/(1 + r^2)$, where $r = E_y/E_x$, and the photon flux $F \propto E_x^2 + E_y^2$. The angular distribution of the final formula is obtained as follows:

$$P = (2\chi)/(1 + \chi^2)^{1/2}*K_{1/3}(\xi)/K_{2/3}(\xi) *[1 + \chi^2/(1 + \chi^2)*K^2{}_{1/3}(\xi)/K^2{}_{2/3}(\xi)]^{-1} \quad (9)$$

$$F = \text{const}*(1 + \chi^2)^2K^2{}_{2/3}(\xi)[K^2{}_{2/3}(\xi) + \chi^2/(1 + \chi^2)K^2{}_{1/3}(\xi)] \quad (10)$$

In the formulas, $K_n(x)$ is the nth-order Bessel function, ψ is the observation angle in the vertical plane, ε is photon energy (854 eV for L_3-Ni^{II}), ε_C is the critical energy (SSRL = 4.72 KeV), $y = \varepsilon/\varepsilon_C = 0.1809$, γ is the ratio of electron energy/rest energy (SSRL = 5870.84), $\chi = \gamma\psi$, and $\xi = y(1 + \chi^2)^{2/3}/2$. As it is a standard calculation, we omit further details.[33] The calculated polarization (solid red line) and intensity (solid green line) are also shown in Figure 7. Our polarization and intensity curves are in close agreement with the previous TEY measurement for this beamline on ferromagnetic samples.[39] The least-squares fit of the measured XMCD data to calculated polarization with two adjustable parameters, the XMCD scaling factor and mirror position offset, gives an almost-perfect agreement in the aspect of the polarization. The discrepancy in the intensity curve is

dx.doi.org/10.1021/jp3027622 | J. Phys. Chem. A 2012, 116, 10082−10089

understandable because once the mirror is moved out of its optimal position, the beam may encounter more intensity cutoff by slits than theoretically predicted.

4. CONCLUSIONS

XMCD spectra have been recorded for the well-defined Ni^{II} and Mn^{II} doped into a single crystal MgO under a sub-Kelvin temperature (0.5 K) using a very high magnetic field (B = 2 T) and with X-ray fluorescence measurements. The fluorescence-detected L-edge absorption spectrum of Ni^{II} in MgO has been comparable with the TEY measurements of Ni^{II} L-edge absorption spectra in similar systems (with a similar octahedral crystal field).[17,26,27] The fluorescence-detected XMCD also shows little difference between the two cases (Table 1), at least qualitatively validating the use of this sensitive technique for the study of a dilute later 3d transition-metal matrix, such as the various biological samples.

Large XMCD effects have been observed for both Ni^{II} and Mn^{II}, and the multiplet simulations have reproduced the observed XMCD with multplet simulations. Meanwhile, XMCD sum rule analyses have also yielded comparable results, showing that X-ray fluorescence-detected XMCD is similar to the total electron yield detected XMCD on similar Ni^{II} site. XMCD measurements have also been utilized to obtain and understand the sample's magnetization curve (as a function of the B/T) and the beamline's helicity curve (as a function of the X-ray takeoff angle). These measurements are also very comparable with theoretical calculations and with the reported TEY measurements.

Although, nowadays, use of an elliptically polarized undulator beamline for XMCD experiments is a trend, this work has illustrated well that a bent magnet beamline is still useful and practical for performing XMCD measurements even for dilute samples.

AUTHOR INFORMATION

Corresponding Author

*To whom correspondence should be addressed.

Present Address

[§]IBM Almaden Research Center, 650 Harry Road, San Jose, California 95120, United States.

Notes

The authors declare no competing financial interest.

ACKNOWLEDGMENTS

This research was supported by the National Institutes of Health (GM-65440) and by the Department of Energy, Office of Environmental Research (ABEX Program). The Stanford Synchrotron Radiation Laboratory (SSRL) and the Advanced Light Source (ALS) are supported by the Department of Energy, Office of Basic Energy Sciences. The LBNL work is under the DOE/LBNL contract DE-AC02-05CH11231.

REFERENCES

(1) Chakarian, V.; Idzerda, Y. U.; Meigs, G.; Chen, C. T. *IEEE Trans. Magn.* **1995**, *31*, 3307.

(2) Stohr, J.; Konig, H. *Phys. Rev. Lett.* **1995**, *75*, 3748.

(3) Stohr, J.; Nakajima, R. *J. Phys. IV* **1997**, *7*, 47.

(4) Cramer, S. P.; Ralston, C. Y.; Wang, H. X.; Bryant, C. *J. Electron Spectrosc. Relat. Phenom.* **1997**, *86*, 175.

(5) Stohr, J.; Padmore, H. A.; Anders, S.; Stammler, T.; Scheinfein, M. R. *Surf. Rev. Lett.* **1998**, *5*, 1297.

(6) Weller, D.; Samant, M. G.; Stohr, J.; Wu, Y.; Hermsmeier, B. D.; Held, G.; Chappert, C. *J. Appl. Phys.* **1994**, *75*, 5807.

(7) Vanderlaan, G.; Thole, B. T. *Phys. Rev. B: Condens. Matter Mater. Phys.* **1991**, *43*, 13401.

(8) Vanderlaan, G.; Thole, B. T. *Phys. Rev. B: Condens. Matter Mater. Phys.* **1995**, *52*, 15355.

(9) Thole, B. T.; Durr, H. A.; Vanderlaan, G. *Phys. Rev. Lett.* **1995**, *74*, 2371.

(10) Groot, F. M. F. d. *Chem. Rev.* **2001**, *101*, 1779.

(11) Groot, F. M. F. d.; Fuggle, J. C.; Thole, B. T.; Sawatzky, G. A. *Phys. Rev. B: Condens. Matter Mater. Phys.* **1990**, *42*, 5459.

(12) Carra, P.; Thole, B. T.; Altarelli, M.; Wang, X. D. *Phys. Rev. Lett.* **1993**, *70*, 694.

(13) Thole, B. T.; Carra, P.; Sette, F.; Vanderlaan, G. *Phys. Rev. Lett.* **1992**, *68*, 1943.

(14) Matsuda, Y. H.; Ouyang, Z. W.; Nojiri, H.; Inami, T.; Ohwada, K.; Suzuki, M.; Kawamura, N.; Mitsuda, A.; Wada, H. *Phys. Rev. Lett.* **2009**, *103*, 046402.

(15) Brossard, S.; Volatron, F.; Lisnard, L.; Arrio, M.-A.; Catala, L.; Mathonire, C.; Mallah, T.; Moulin, C. C. d.; Rogalev, A.; Wilhelm, F.; Smekhova, A.; Sainctavit, P. *J. Am. Chem. Soc.* **2011**, *134*, 222.

(16) Cramer, S. P.; Chen, J.; George, S. J.; Elp, J. v.; Moore, J.; Tensch, O.; Colaresi, J.; Yocum, M.; Mullins, O. C.; Chen, C. T. *Nucl. Instrum. Methods Phys. Res., Sect. A* **1992**, *319*, 285.

(17) Wang, H. X.; Bryant, C.; Randall, D. W.; LaCroix, L. B.; Solomon, E. I.; LeGros, M.; Cramer, S. P. *J. Phys. Chem. B* **1998**, *102*, 8347.

(18) Funk, T.; Deb, A.; George, S. J.; Wang, H. X.; Cramer, S. P. *Coord. Chem. Rev.* **2005**, *249*, 3.

(19) Finkelstein, J. *Nature* **2009**, *460*, 813.

(20) Wang, H. X.; Peng, G.; Miller, L. M.; Scheuring, E. M.; George, S. J.; Chance, M. R.; Cramer, S. P. *J. Am. Chem. Soc.* **1997**, *119*, 4921.

(21) Wang, H. X.; Ralston, C. Y.; Patil, D. S.; Jones, R. W.; Gu, W.; Verhagen, M.; Adams, M. W. M.; Ge, P. H.; Riordan, C.; Marganian, C. A.; Mascharak, P.; Kovacs, J.; Miller, C. G.; Collins, T. J.; Brooker, S.; Croucher, P. D.; Wang, K.; Stiefel, E. I.; Cramer, S. P. *J. Am. Chem. Soc.* **2000**, *122*, 10544.

(22) Groot, F. M. F. d.; Arrio, M. A.; Sainctavit, P.; Cartier, C.; Chen, C. T. *Phys. B* **1995**, *209*, 84.

(23) Groot, F. M. F. d.; Fuggle, J. C.; Thole, B. T.; Sawatzky, G. A. *Phys. Rev. B: Condens. Matter Mater. Phys.* **1990**, *41*, 928.

(24) Veenendaal, M. v.; Goedkoop, J. B.; Thole, B. T. *Phys. Rev. Lett.* **1996**, *77*, 1508.

(25) Orton, J. W.; Auzins, P.; Wertz, J. W. *Phys. Rev. Lett.* **1960**, *4*, 128.

(26) Arrio, M. A.; Sainctavit, P.; Moulin, C. C. D.; Brouder, C.; Groot, F. M. F. d.; Mallah, T.; Verdaguer, M. *J. Electron Spectrosc. Relat. Phenom.* **1996**, *78*, 203.

(27) Arrio, M. A.; Sainctavit, P.; Moulin, C. C. D.; Brouder, C.; Groot, F. M. F. d.; Mallah, T.; Verdaguer, M. *Phys. B* **1995**, *209*, 775.

(28) Xiao, Y. M.; Wang, H. X.; George, S. J.; Smith, M. C.; Adams, M. W. M.; Jenney, F. E.; Sturhahn, W.; Alp, E. E.; Zhao, J. Y.; Yoda, Y.; Dey, A.; Solomon, E. I.; Cramer, S. P. *J. Am. Chem. Soc.* **2005**, *127*, 14596.

(29) Feng, W. L.; Li, X. M.; Yang, W. J.; Tao, C. Y.; Yang, Y. L. *Optik* **2011**, *122*, 1512.

(30) Lounasmaa, O. V. *Experimental Principles and Methods below 1K*; Academic Press: London, 1974.

(31) Terminello, L. J.; Waddill, G. D.; Tobin, J. G. *Nucl. Instrum. Methods Phys. Res., Sect. A* **1992**, *319*, 271.

(32) Tirsell, K. G.; Karpenko, V. P. *Nucl. Instrum. Methods Phys. Res., Sect. A* **1990**, *291*, 511.

(33) Margaritondo, G. *Introduction to Synchrotron Radiation*; Oxford University Press: New York, 1988.

(34) Rossano, S.; Brouder, C.; Alouani, M.; Arrio, M. A. *Phys. Chem. Miner.* **2000**, *27*, 170.

(35) Pompa, M.; Flank, A. M.; Lagarde, P.; Rife, J. C.; Stekhin, I.; Nakazawa, M.; Ogasawara, H.; Kotani, A. *Phys. Rev. B: Condens. Matter Mater. Phys.* **1997**, *56*, 2267.

(36) Pompa, M.; Flank, A. M.; Delaunay, R.; Bianconi, A.; Lagarde, P. *Phys. B* **1995**, *209*, 143.
(37) Wang, H. X.; Ge, P. H.; Riordan, C. G.; Brooker, S.; Woomer, C. G.; Collins, T.; Melendres, C. A.; Graudejus, O.; Bartlett, N.; Cramer, S. P. *J. Phys. Chem. B* **1998**, *102*, 8343.
(38) Rudolf, P.; Sette, F.; Tjeng, L. H.; Meigs, G.; Chen, C. T. *J. Magn. Magn. Mater.* **1992**, *109*, 109.
(39) Nakajima, R. *X-ray Magnetic Circular Dichroism of 3d Transition Metals*; Stanford University: Stanford, CA, 1997.
(40) Barbara, B.; Gignoux, G. *Lectures on Modern Magnetism*; Springer-Verlag: New York, 1988; Vol. *1988*.